

Momentum-Space Josephson Effects

Junpeng Hou,¹ Xi-Wang Luo,¹ Kuei Sun,¹ Thomas Bersano,² Vandna Gokhroo,² Sean Mossman,² Peter Engels,² and Chuanwei Zhang^{1,*}

¹*Department of Physics, The University of Texas at Dallas, Richardson, Texas 75080-3021, USA*

²*Department of Physics and Astronomy, Washington State University, Pullman, WA 99164, USA*

The Josephson effect is a prominent phenomenon of quantum supercurrents that has been widely studied in superconductors and superfluids. Typical Josephson junctions consist of two real-space superconductors (superfluids) coupled through a weak tunneling barrier. Here we propose a momentum-space Josephson junction in a spin-orbit coupled Bose-Einstein condensate, where states with two different momenta are coupled through Raman-assisted tunneling. We show that Josephson currents can be induced not only by applying the equivalent of “voltages”, but also by tuning tunneling phases. Such *tunneling-phase-driven Josephson junctions* in momentum space are characterized through both full mean field analysis and a concise two-level model, demonstrating the important role of interactions between atoms. Our scheme provides a platform for experimentally realizing momentum-space Josephson junctions and exploring their applications in quantum-mechanical circuits.

Introduction. The Josephson effect [1, 2] is an intriguing quantum phenomenon of supercurrents across a device known as a Josephson junction (JJ). A typical JJ consists of two macroscopic quantum systems [e.g., superconductors, superfluids, or Bose-Einstein condensates (BECs)] that are separated in real or spin space and weakly coupled by quantum tunneling through a thin barrier [Fig. 1(a)] or by Rabi coupling between different spins. Because of quantum tunneling of particles across the junction, JJs have found important applications in quantum-mechanical circuits, such as SQUIDS [3, 4], superconducting qubits [5–8], and precision measurements [3]. In experiments, JJs have been widely realized in solid state superconductors [9, 10], superfluid Helium [11–14], and recently, in ultra-cold atomic gases [15–26], where oscillating supercurrents were generated by applying a voltage drop (or its equivalent) across JJs while maintaining a constant weak coupling (*i.e.*, a.c. Josephson effect [27]).

While JJs have been well studied in real space, a natural and important question is whether Josephson effects can also be observed in momentum space. In this paper, we address this question and propose a scheme for realizing momentum-space JJs (MSJJs). In analogy to bosonic JJs in a real-space double well [22, 23], a MSJJ may be realized with a momentum-space double-well dispersion [see Fig. 1(a)], which is an essential property of spin-orbit coupled systems [28, 29]. Spin-orbit coupling (SOC) is ubiquitous in solid state materials and has recently been realized experimentally in ultracold atomic gases [29–41]. In the presence of SOC, condensates at distinct band minima can be considered as two distinct independent quantum systems. However, unlike quantum tunneling between two wells in real space, two BECs at distinct momenta are not directly coupled.

Here we propose a MSJJ facilitated by a tunable interwell coupling in an spin-orbit coupled BEC [42, 43], where the coupling is generated by an additional pair of counter-propagating Raman lasers. Such Raman-assisted

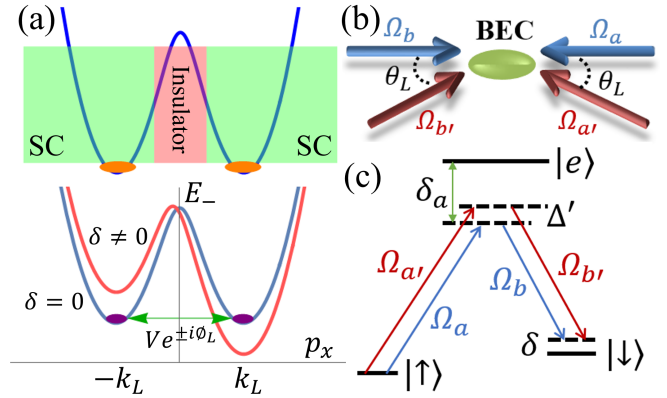


FIG. 1: (a) Illustration of conventional JJ for real-space superconductors (top) versus MSJJ (bottom), where the double well band dispersion is generated using a spin-orbit coupled BEC. (b,c) Experimental setup for realizing a MSJJ. Two pairs of Raman lasers realize SOC (blue) and weak coupling (red) between two band minima, respectively.

tunneling between two momentum states changes both the atomic spin and momentum, and thus couples the condensates at the two band minima. The SOC coupling strength dictates the height of the insulating barrier while the Raman detuning serves as an effective voltage between the two band minima. Suddenly changing the detuning (*i.e.*, applying a voltage) induces a coherent oscillation of the BECs between the two band minima (*i.e.*, supercurrent oscillations), similar to traditional a.c. Josephson effects in superconductors. More interestingly, the phase of the Raman-assisted tunneling between BECs at the two band minima is highly tunable [44], in contrast to real tunneling coefficients for real-space JJs in superconductors [9, 10] and double-well BECs [22, 23]. We show that a sudden change of the tunneling phase (while keeping the effective voltage unchanged) can also induce Josephson effects of supercurrents, a phenomenon

that we name as “*tunneling-phase-driven JJ*”. We focus on this new type of Josephson effect and study its properties through both full mean-field simulation with the Gross-Pitaevskii equation (GPE) [15, 45] and the development of an effective two-level model. Our results present rich physics in this system with different types of supercurrent oscillations (Josephson, plasmonic [17], self-trapping [17, 22], etc.) and display the important role of many-body interactions between atoms. Due to their stability and high controllability, the proposed MSJJs and tunneling-phase-driven JJs may have potential applications for building novel quantum mechanical circuits.

Experimental setup and theoretical modeling. We consider a BEC confined in an elongated trap. Two internal states $|\uparrow\rangle$ and $|\downarrow\rangle$ are coupled by two counter-propagating Raman lasers with Rabi frequencies Ω_a and Ω_b , forming an effective one-dimensional (1D) SOC dispersion relation along the x direction [see Fig. 1(b, c)]. Hereafter we choose recoil momentum $\hbar k_R$ and recoil energy $E_R = \hbar^2 k_R^2 / 2m$ for the Raman lasers as the units of momentum and energy. Consequently, we have length and time in units of $2\pi/k_R$ and \hbar/E_R . The 1D SOC displays a double-well band dispersion in momentum space with two band minima located at $\pm k_L = \pm\sqrt{1 - (\Omega/4)^2}$, where Ω is the Raman coupling strength [46]. The tunneling between BECs at $\pm k_L$ requires simultaneous change of spin and momentum, which can be realized using another independent pair of Raman lasers $\Omega_{a'}$ and $\Omega_{b'}$ incident at an angle $\theta_L = \arccos(1 - k_L)$ to the x axis [Fig. 1(b)]. The frequencies of the pair (a', b') are shifted from those of the pair (a, b) by $\Delta' \sim 100$ MHz so that the interference between them is negligible. The frequency difference between a' and b' should match that between a and b to generate a time-independent coupling.

Since only the x direction is relevant for the SOC dynamics, the other two directions can be integrated out, yielding an effective 1D system. The dynamics of the system can be described by the GPE

$$i \frac{\partial}{\partial t} \psi = (H_0 + \frac{1}{2} \omega_x^2 x^2 + \frac{g}{2} |\psi|^2) \psi \quad (1)$$

under the mean-field approximation, where $\psi = (\psi_\uparrow, \psi_\downarrow)^T$ is the two component condensate wavefunction normalized by the average particle number density $n = \int dx \psi^\dagger \psi$, ω_x represents trapping frequency of harmonic trap. For a typical ^{87}Rb BEC, the effective density interaction $ng \sim 0.1$ with $\sim 10^4$ atoms (see “Experimental consideration” section) and the spin interaction is negligible. The Raman coupling does not affect atomic interactions. The single particle Hamiltonian can be written as [47, 49]

$$H_0 = \begin{pmatrix} (p_x - 1)^2 - \frac{\delta}{2} & \frac{\Omega}{2} + e^{i\phi_L} \Omega_L e^{2ik_L x} \\ \frac{\Omega}{2} + e^{-i\phi_L} \Omega_L e^{-2ik_L x} & (p_x + 1)^2 + \frac{\delta}{2} \end{pmatrix}, \quad (2)$$

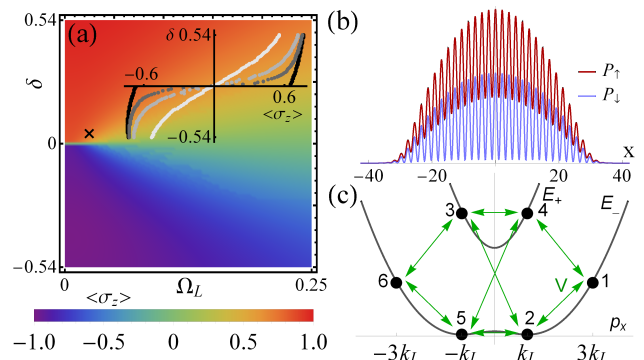


FIG. 2: (a) Ground state phase diagram, where $\Omega = 2.7$, $\phi_L = 0$ and $ng = 0.07$. The inset shows the first-order phase transition for small Ω_L . Black, dark gray, light gray and white lines correspond to $\Omega_L = 0.01, 0.1, 0.2$ and 0.5 respectively. (b) Real space density modulation for the ground state with parameters $\delta = 0.054$ and $\Omega_L = 0.015$ as denoted by the black cross in (a). (c) Illustration of induced couplings between six most relevant momentum states.

where Ω_L is the coupling strength generated by the tunneling lasers, ϕ_L is the relative phase between the two Raman couplings, and δ is the detuning.

The ground state of the BEC is obtained from the imaginary time evolution of the GPE [47, 50] using a time-split-operator method, resulting in the phase diagram shown in Fig. 2(a) in the Ω_L - δ plane, where the color represents spin polarization $\langle \sigma_z \rangle$. For weak Ω_L , interactions lock the condensate to one momentum minimum, yielding a plane-wave phase at large detunings. There is a first-order phase transition [black line in the inset of Fig 2(a)] when δ crosses 0. With increasing Ω_L , the single-particle coupling dominates over the interaction, hence the ground state is in a stripe-like phase with a real-space density modulation [Fig. 2(b)], and $\langle \sigma_z \rangle$ varies continuously and smoothly with respect to δ (white line in the inset of Fig. 2(a)). While a supersolid stripe phase is defined through spontaneous breaking of both continuous translational and gauge symmetries [51, 52], here continuous translational symmetry is synthetically broken by the periodic potential $e^{2ik_L x}$. Nevertheless, the ground state is the superposition of two band minima, similar to an authentic stripe phase induced by interactions.

The additional Raman lasers Ω_L couple not only the two band minima, but also other states from both lower and upper bands. The six most relevant momentum states ψ_i are shown in Fig. 2(c). Expanding the wavefunction $\psi = \sum_{i=1}^6 C_i \psi_i$ in this six-state basis, we obtain a 6×6 effective Hamiltonian [47]. The direct coupling between the two band minima at 2 and 5 is $-V_0 e^{\mp i\phi_L}$ with $V_0 = \frac{1}{2} \Omega_L (1 + k_L)$, while the couplings with other neighboring high-energy states are $-\sqrt{\frac{1-k_L}{2}} e^{\pm i\phi_L}$ and $\frac{1}{2} \sqrt{1 - k_L^2} e^{\mp i\phi_L}$, which approach 0 when $k_L \rightarrow 1$, leav-

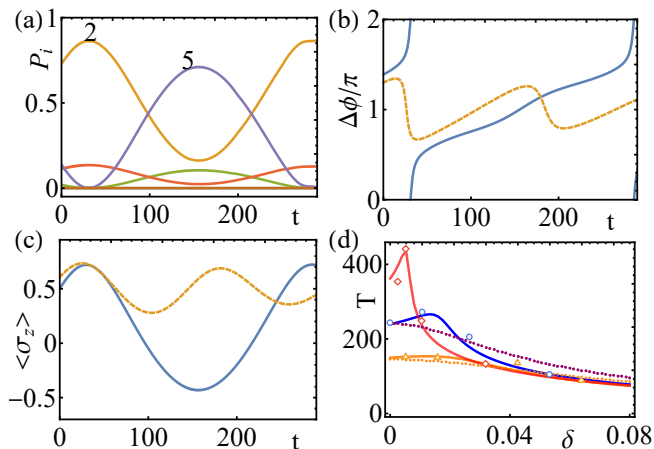


FIG. 3: (a) Time evolution of the populations at different momentum states for tunneling-phase-driven MSJJ for $\Omega = 2.7$, $\delta = 0.014$, $\Omega_L = 0.015$ and $ng = 0.07$. (b) and (c): Evolutions of phase difference (b) and polarization (c) for Josephson oscillation (solid blue) and plasma oscillation (dashed orange). (d) Oscillation period T versus δ when ϕ_L is quenched from ϕ_{L0} to 0 at $\Omega = 2.7$. Circles are results from the GPE simulation, while solid ($ng = 0.07$) and dashed (single particle) lines are from the two-level model. Different colors correspond to different parameter sets: $\Omega_L = 0.015$, $\phi_{L0} = 0.4\pi$ (blue); $\Omega_L = 0.025$, $\phi_{L0} = 0.4\pi$ (orange); and $\Omega_L = 0.015$, $\phi_{L0} = 0.2\pi$ (red). Blue and red dashed lines overlap (purple) since T is independent of ϕ_{L0} for the single particle case.

ing V_0 as the dominant tunneling term. We focus on the region $\Omega_L \ll \Omega$ to avoid significant modification of the original SOC band dispersion and also for the observation of Josephson effects with weak tunneling.

Tunneling-phase-driven MSJJ. In an a.c. JJ, a suddenly applied voltage can induce an oscillation of supercurrents between two superconductors. In our system, BECs at the two band minima marked 2 and 5 are considered as two superfluids and the detuning between them corresponds to a voltage. A sudden change of δ induces an oscillation of the BEC between the two minima, yielding a MSJJ whose properties are described in the supplementary materials [47]. Here we focus on the relative phase ϕ_L for the tunneling element between 2 and 5, which is highly tunable in experiments [44]. In contrast, such tunneling is a real number for a real space JJ between two superconductors or double well BECs. A sudden change of the phase ϕ_L (keeping δ constant) can induce a different type of Josephson effect, *i.e.*, *tunneling-phase-driven JJ*.

In Figs. 3(a)–(c) we show dynamics from simulations of the GPE with a sudden change of the phase ϕ_L from an initial ϕ_{L0} to $\phi_{Lf} = 0$. In panel (a) we plot the population $P_i(t)$ at each momentum state for $\phi_{L0} = 0.4\pi$. Clearly only the states 2 and 5 at the two band minima are largely populated while all other states can be neglected due to their small initial populations, weak cou-

pling to states 2 and 5, and high energies. Panel (b) shows the relative phase between BECs in states 2 and 5. For $\phi_{L0} = 0.4\pi$ (blue solid line), the phase varies through $[0, 2\pi)$, representing a Josephson type of oscillation; while for $\phi_{L0} = 0.3\pi$ (yellow dashed line), the phase oscillates in a small range, showing a plasma oscillation. The polarization $\langle\sigma_z\rangle$ exhibits sinusoidal oscillations for both cases [panel (c)].

Because the population of the BEC stays mainly at the two band minima 2 and 5, we can neglect the other states to derive an effective two-level model, yielding an equation of motion [46, 47]

$$i\partial_t \begin{pmatrix} C_2 \\ C_5 \end{pmatrix} = (H_0^{\text{eff}} + H_1^{\text{eff}}) \begin{pmatrix} C_2 \\ C_5 \end{pmatrix}, \quad (3)$$

where $H_0^{\text{eff}} = \begin{pmatrix} -k_L\delta & -V_0e^{-i\phi_L} \\ -V_0e^{i\phi_L} & k_L\delta \end{pmatrix}$ is the effective single-particle Hamiltonian, and $H_1^{\text{eff}} = 2g_G \begin{pmatrix} |C_5|^2 & 0 \\ 0 & |C_2|^2 \end{pmatrix}$ is the effective interaction term obtained through a variational approximation of the GPE. Generally, g_G depends on $|C_2|^2|C_5|^2$ but is approximately a constant when the interaction strength is weak compared to E_R , yielding $g_G = ng(1 - k_L^2)$. Note that the coupling phase ϕ_L in Eq. (3) can be incorporated into the relative phase between C_2 and C_5 through a simple phase transformation, therefore the quench of ϕ_L is mathematically equivalent to a quench of the relative phase between condensates at two minima (2, 5), although the latter is experimentally impractical.

When the coupling V_0 is strong, the dynamics of the BEC are governed by single particle physics, yielding a linear Rabi oscillation with period $T = \pi/\omega$, where the Rabi frequency $\omega = \sqrt{(k_L\delta)^2 + |V_0|^2}$. Such a simple formula for the period does not apply when the tunneling V_0 is comparable to or weaker than the inter-particle interactions, although the two-level model still agrees reasonably well with the GPE simulations, as shown in Fig. 3(d). We see that the period is similar for interacting and single-particle cases for a large coupling $\Omega_L = 0.025$, but shows strong deviations [see the sharp peak for the solid red line in Fig. 3(d)] from the single particle curve for $\Omega_L = 0.015$. For a very large detuning δ (*i.e.*, voltage), all T collapse to the same line as the single particle case, as expected.

In the two-level approximation, we can choose the normalization $|C_2|^2 + |C_5|^2 = 1$, and recast the equation of motion (3) as [47]

$$\begin{aligned} \partial_t z &= -\sqrt{1 - z^2} \sin(\phi - \phi_{Lf}), \\ \partial_t \phi &= \frac{g_G}{V_0} z + \frac{z}{\sqrt{1 - z^2}} \cos(\phi - \phi_{Lf}) + \frac{k_L\delta}{V_0}, \end{aligned} \quad (4)$$

using the population difference $z = (N_2 - N_5)/N$ and relative phase $\phi = \theta_2 - \theta_5$, where N_i and θ_i are defined

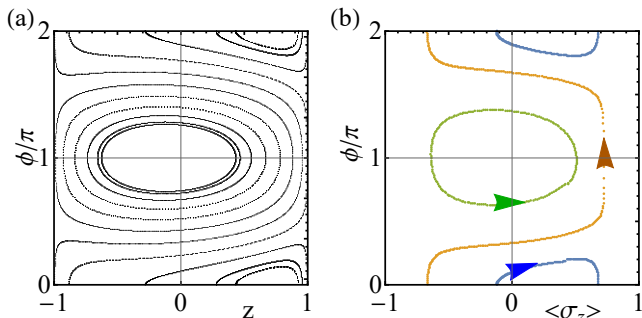


FIG. 4: (a) Classical trajectories in z - ϕ plane for $0 < \phi_{L0} \leq \pi$, with initial value of z at 0.434. (b) Same as (a) but generated through the GPE simulation. Parameters are $ng = 0.07$, $\delta = 0.008$ (corresponding to initial polarization 0.434), $\Omega = 2.7$ and $\Omega_L = 0.015$. The three colors correspond to $\phi_{L0} = 0.2$ (blue), 0.4 (orange), 0.8 (green), respectively. The arrows denote the direction of each trajectory.

through $C_2 = \sqrt{N_2}e^{i\theta_2}$ and $C_5 = \sqrt{N_5}e^{i\theta_5}$. These two classical equations characterize the essential dynamics of MSJJs.

Fig. 4(a) shows how the initial value ϕ_{L0} affects the dynamics. For a relatively small ϕ_{L0} , the classical trajectory is a closed loop around a fixed point with a small amplitude of z and a confined range of phase change $\Delta\phi$, showing a plasma oscillation [17]. With increasing ϕ_{L0} , the amplitudes for both ϕ and z increase. Beyond a critical ϕ_{L0} , ϕ varies through $[0, 2\pi)$, showing a Josephson oscillation. The system returns to plasma oscillation around another fixed point when ϕ_{L0} exceeds another critical point. These classical trajectories from the two-level model agree with those from the GPE simulations in Fig. 4(b). Note that the trajectories around two fixed points have opposite directions. In the single-particle case, these two fixed points correspond to two opposite Zeeman fields for spin precession of the Rabi oscillation [47].

Strong interaction between atoms can dramatically change the BEC dynamics and lead to a self-trapping effect [17, 22], where the oscillation amplitude of z is strongly suppressed. We consider a symmetric oscillation with $\delta = 0$. For a weak interaction of $ng = 0.07$, the oscillation of $\langle\sigma_z\rangle$ shows a perfect sinusoidal pattern (blue line), as seen by the blue line Fig. 5(a) obtained from the GPE simulation. When the interaction is doubled $ng = 0.14$, the oscillation amplitude is reduced and the average $\langle\sigma_z\rangle$ in one period changes from 0 to a finite value (orange line). For a larger but still practicable interaction of $ng = 0.35$, the oscillatory behavior disappears and the condensate is locked at the initial band minimum because of strong density interaction. Such nonlinear self-trapping effects can also be captured in the classical trajectories in the two-level model [Fig. 5 (b)]. With increasing ng , the initial plasma oscillation with a

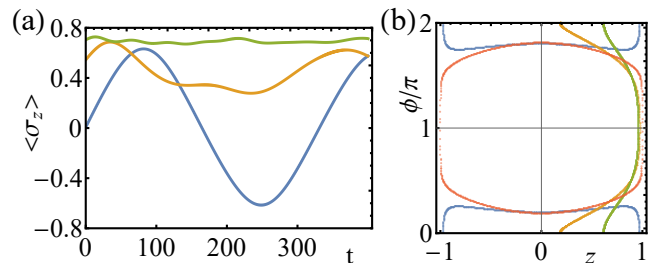


FIG. 5: (a) Self-trapping effects from the GPE simulation. The curves correspond to $ng = 0.07$ (blue), 0.14 (orange) and 0.35 (green), for $\Omega = 2.7$, $\Omega_L = 0.03$, $\phi_{L0} = 0.2\pi$ and $\delta = 0$. (b) Classical phase-plane from the two-level model. The colors are the same as in (a) except $ng = 0.1$ for the red curve.

large variation of z becomes the self-trapped Josephson oscillation with a small z change.

Experimental consideration. The periodic density modulation for the stripe-like ground state can be measured using Bragg scattering, similar to the recent experiments for observing supersolid stripe phases [53]. Consider a ^{87}Rb BEC confined in a quasi-1D harmonic trap. The Raman lasers for generating SOC are incident at 45° with the x axis, yielding an effective wavevector $k_R = \frac{2\pi}{\sqrt{2}\lambda}$ with $\lambda = 784$ nm. The corresponding recoil energy $E_R = 2\pi\hbar \times 1.8$ kHz, thus the time and length units are $\hbar/E_R = 0.088$ ms and $2\pi/k_R = 1109$ μm , respectively. The Raman coupling strength for SOC $\Omega = 2.7E_R$, thus $k_L = 0.738k_R$ and the second pair of Raman lasers should be incident at an angle $\theta_L = 58.6^\circ$ with respect to the x axis. The s-wave scattering length of ^{87}Rb is $a_s = 100.86a_0$, where a_0 is the Bohr radius. Considering a particle number 10^4 to 10^6 and typical trapping frequencies $\omega_x \sim 2\pi \times 5$ Hz and $\omega_y = \omega_z \sim 2\pi \times 75$ Hz, one has the average particle density $n \sim 10^{13}$ to 10^{14} cm^{-3} under Thomas-Fermi approximation [45]. The effective interaction strength can be evaluated through $ng = 4\pi\hbar^2 a_s n / m \sim 0.07$ to $0.48 E_R$, resulting in the time period $T \sim 10$ ms for tunneling-phase-driven Josephson oscillations [Fig. 3(d)].

Discussion and Conclusion. Our two major proposed concepts, momentum-space JJ and tunneling-phase-driven JJ, may also be realized in other physical systems where a double well band dispersion with two almost degenerate local band minima can be generated to ensure the long life time of the BEC at different momenta [54]. For instance, the double-well band dispersion may be realized in optical superlattices with Raman assisted tunneling [55], where two momentum minima can be coupled with additional Raman transitions. The double-well band dispersion can be generalized to triple-well or even more multiple-degenerate momentum states, and the coupling between neighboring minima may form a momentum-space optical lattice [54], which

can be considered as a Josephson junction array [20] in momentum space. The linear momentum discussed here can be generalized to orbital angular momentum (OAM), and an OAM-space JJ may be realized for a BEC on a ring utilizing recent proposals for spin-OAM coupling [56–58] for cold atoms. The discreteness of OAM states may induce interesting Josephson effects that are different from those in continuous real or momentum space. Finally, although absent in solid-state superconductors, the proposed tunneling-phase-induced JJ may be realized in real-space optical superlattices with Raman assisted tunneling [55], where the phase for the Raman tunneling may also be tuned.

In conclusion, we propose a new category of Josephson effects in momentum space, which can be built in a spin-orbit coupled BEC. In addition to traditional voltage-driven Josephson effects, we introduce quenching of the tunneling phase as a novel driving mechanism. Our work may motivate further experimental and theoretical works for studying MSJJs and provides a platform for exploring their applications in building novel quantum mechanical circuits.

Acknowledgements: This work was supported by Air Force Office of Scientific Research (FA9550-16-1-0387), National Science Foundation (PHY-1505496), and Army Research Office (W911NF-17-1-0128). P. E. acknowledges funding from National Science Foundation (PHY-1607495).

* Corresponding author.

Email: chuanwei.zhang@utdallas.edu

- [1] B.D. Josephson, Possible new effects in superconductive tunnelling, *Phys. Rev. Lett.* **1**, 251 (1962).
- [2] B.D. Josephson, The discovery of tunnelling supercurrents, *Rev. Mod. Phys.* **46**, 251 (1974).
- [3] Y. Makhlin, G. Schon, and A. Shnirman, Quantum-state engineering with Josephson-junction devices, *Rev. Mod. Phys.* **73**, 357 (2001).
- [4] C. Ryu, P. W. Blackburn, A. A. Blinova, and M. G. Boshier, Experimental Realization of Josephson Junctions for an Atom SQUID, *Phys. Rev. Lett.* **111**, 205301 (2013).
- [5] J. M. Martinis, S. Nam, J. Aumentado, and C. Urbina, Rabi Oscillations in a Large Josephson-Junction Qubit, *Phys. Rev. Lett.* **89**, 117901 (2002).
- [6] O. Astafiev, Y. A. Pashkin, Y. Nakamura, T. Yamamoto, and J. S. Tsai, Temperature Square Dependence of the Low Frequency $1/f$ Charge Noise in the Josephson Junction Qubits, *Phys. Rev. Lett.* **96**, 137001 (2006).
- [7] J. M. Martinis, M. Ansmann, and J. Aumentado, Energy Decay in Superconducting Josephson-Junction Qubits from Nonequilibrium Quasiparticle Excitations, *Phys. Rev. Lett.* **103**, 097002 (2009).
- [8] H. Paik *et al.*, Observation of High Coherence in Josephson Junction Qubits Measured in a Three-Dimensional Circuit QED Architecture, *Phys. Rev. Lett.* **107**, 240501 (2011).
- [9] I. Giaever, Energy Gap in Superconductors Measured by Electron Tunneling, *Phys. Rev. Lett.* **5**, 147 (1960).
- [10] K. K. Likharev, Superconducting weak links, *Rev. Mod. Phys.* **51**, 101 (1979).
- [11] S. V. Pereverzev, A. Loshak, S. Backhaus, J. C. Davis & R. E. Packard, Quantum oscillations between two weakly coupled reservoirs of superfluid ^3He , *Nature* **388**, 451 (1997).
- [12] E. Hoskinson, R. E. Packard & T. M. Haard, Oscillatory motion: Quantum whistling in superfluid helium-4, *Nature* **433**, 376 (2005).
- [13] J. C. Wheatley, Experimental properties of superfluid ^3He , *Rev. Mod. Phys.* **47**, 415 (1975).
- [14] A. J. Leggett, A theoretical description of the new phases of liquid ^3He , *Rev. Mod. Phys.* **47**, 331 (1975).
- [15] F. Dalfovo, S. Giorgini, L. P. Pitaevskii, and Stringari, S., Theory of Bose-Einstein condensation in trapped gases, *Rev. Mod. Phys.* **71**, 463 (1999).
- [16] A. Smerzi, S. Fantoni, S. Giovanazzi, and S. R. Shenoy, Quantum Coherent Atomic Tunneling between Two Trapped Bose-Einstein Condensates, *Phys. Rev. Lett.* **79**, 4950 (1997).
- [17] S. Raghavan, A. Smerzi, S. Fantoni, and S. R. Shenoy, Coherent oscillations between two weakly coupled Bose-Einstein condensates: Josephson effects, π oscillations, and macroscopic quantum self-trapping, *Phys. Rev. A* **59**, 620 (1999).
- [18] J. Williams, R. Walser, J. Cooper, E. Cornell, and M. Holland, Nonlinear Josephson-type oscillations of a driven, two-component Bose-Einstein condensate, *Phys. Rev. A* **59**, R31(R) (1999).
- [19] P. Ohberg and S. Stenholm, Internal Josephson effect in trapped double condensates, *Phys. Rev. A* **59**, 3890 (1999).
- [20] F. S. Cataliotti *et al.*, Josephson Junction Arrays with Bose-Einstein Condensates, *Science* **293**, 843 (2001).
- [21] T. Zibold, E. Nicklas, C. Gross, and M. K. Oberthaler, Classical Bifurcation at the Transition from Rabi to Josephson Dynamics, *Phys. Rev. Lett.* **105**, 204101 (2010).
- [22] M. Albiez *et al.*, Direct Observation of Tunneling and Nonlinear Self-Trapping in a Single Bosonic Josephson Junction, *Phys. Rev. Lett.* **95**, 010402 (2005).
- [23] S. Levy, E. Lahoud, I. Shomroni & J. Steinhauer, The a.c. and d.c. Josephson effects in a Bose-Einstein condensate, *Nature* **449**, 579 (2007).
- [24] G. Valtolina *et al.*, Josephson effect in fermionic superfluids across the BEC-BCS crossover, *Science*, **350**, 1505 (2015).
- [25] A. Burchianti *et al.*, Connecting dissipation and phase slips in a Josephson junction between fermionic superfluids, *Phys. Rev. Lett.* **120**, 025302 (2018).
- [26] A. Burchianti, C. Fort, and M. Modugno, Josephson plasma oscillations and the Gross-Pitaevskii equation: Bogoliubov approach versus two-mode model, *Rev. Phys. A* **95**, 023627 (2017).
- [27] P. W. Anderson, Chapter I The Josephson Effect and Quantum Coherence Measurements in Superconductors and Superfluids, *Prog. Low Temp. Phys.* **5**, 5 (1967).
- [28] N. Goldman, G. Juzeliunas, P. Ohberg and I. B. Spielman, Light-induced gauge fields for ultracold atoms, *Rep. Prog. Phys.* **77**, 126401 (2014).
- [29] Y.-J. Lin, K. Jiménez-García, and I. B. Spielman, Spin-

- orbit-coupled Bose-Einstein condensates, *Nature (London)* **471**, 83 (2011).
- [30] J.-Y. Zhang *et al*, Collective Dipole Oscillations of a Spin-Orbit Coupled Bose-Einstein Condensate, *Phys. Rev. Lett.* **109**, 115301 (2012).
- [31] C. Qu, C. Hamner, M. Gong, C. Zhang, and P. Engels, Observation of Zitterbewegung in a spin-orbit-coupled Bose-Einstein condensate, *Phys. Rev. A* **88**, 021604(R) (2013).
- [32] A. J. Olson *et al*, Tunable Landau-Zener transitions in a spin-orbit-coupled Bose-Einstein condensate, *Phys. Rev. A* **90**, 013616 (2014).
- [33] C. Hamner *et al*, Dicke-type phase transition in a spin-orbit-coupled Bose-Einstein condensate, *Nat. Commun.* **5**, 4023 (2014).
- [34] P. Wang *et al*, Spin-Orbit Coupled Degenerate Fermi Gases, *Phys. Rev. Lett.* **109**, 095301 (2012).
- [35] L. W. Cheuk *et al*, Spin-Injection Spectroscopy of a Spin-Orbit Coupled Fermi Gas, *Phys. Rev. Lett.* **109**, 095302 (2012).
- [36] R. A. Williams *et al*, Raman-Induced Interactions in a Single-Component Fermi Gas Near an s -Wave Feshbach Resonance, *Phys. Rev. Lett.* **111**, 095301 (2013).
- [37] N. Q. Burdick, Y. Tang, and B. L. Lev, Long-Lived Spin-Orbit-Coupled Degenerate Dipolar Fermi Gas, *Phys. Rev. X* **6**, 031022 (2016).
- [38] B. Song *et al*, Spin-orbit-coupled two-electron Fermi gases of ytterbium atoms, *Phys. Rev. A* **94**, 061604(R) (2016).
- [39] L. Huang *et al*, Experimental realization of two-dimensional synthetic spin-orbit coupling in ultracold Fermi gases, *Nat. Phys.* **12**, 540 (2016).
- [40] Z. Meng *et al*, Experimental Observation of a Topological Band Gap Opening in Ultracold Fermi Gases with Two-Dimensional Spin-Orbit Coupling, *Phys. Rev. Lett.* **117**, 235304 (2016).
- [41] Z. Wu *et al*, Realization of two-dimensional spin-orbit coupling for Bose-Einstein condensates, *Science* **354**, 83 (2016).
- [42] V. Galitski, and I. B. Spielman, Spin-orbit coupling in quantum gases, *Nature* **494**, 49 (2013).
- [43] Y. Zhang, M. E. Mossman, T. Busch, P. Engels, C. Zhang, Properties of spin-orbit-coupled Bose-Einstein condensates, *Front. Phys.* **11**, 118103 (2016).
- [44] K. Jiménez-García *et al*, Tunable Spin-Orbit Coupling via Strong Driving in Ultracold-Atom Systems, *Phys. Rev. Lett.* **114**, 125301 (2015).
- [45] C. J. Pethick and H. Smith, Bose-Einstein Condensation in Dilute Gases, Cambridge University Press (2002).
- [46] Y. Li, L. P. Pitaevskii, and S. Stringari, Quantum Tricriticality and Phase Transitions in Spin-Orbit Coupled Bose-Einstein Condensates, *Phys. Rev. Lett.* **108**, 225301 (2012).
- [47] See Supplementary Materials for derivation of system Hamiltonian, 2-mode model, voltage-driven MSJJ and numerical recipes for GPE simulations, which includes Ref. [48].
- [48] W. Bao, D. Jaksch, P. A. Markowich, Numerical solution of the Gross-Pitaevskii equation for Bose-Einstein condensation, *J. Comput. Phys.* **187**, 318 (2003).
- [49] E. Brion, L. H. Pedersen and K. Mølmer, Adiabatic elimination in a lambda system, *J. Phys. A* **40**, 1033 (2007).
- [50] P. Bader, S. Blanes, and F. Casas, Solving the Schrödinger eigenvalue problem by the imaginary time propagation technique using splitting methods with complex coefficients, *J. Chem. Phys.* **139**, 124117 (2013).
- [51] G. I. Martone, Y. Li, and S. Stringari, Approach for making visible and stable stripes in a spin-orbit-coupled Bose-Einstein superfluid, *Phys. Rev. A* **90**, 041604 (2014).
- [52] G. I. Martone, T. Ozawa, C. Qu, S. Stringari, Optical-lattice-assisted magnetic phase transition in a spin-orbit-coupled Bose-Einstein condensate, *Phys. Rev. A* **94**, 043629 (2016).
- [53] J.-R. Li *et al*, A stripe phase with supersolid properties in spin-orbit-coupled Bose-Einstein condensates, *Nature* **543**, 91 (2017).
- [54] F. A. An, E. J. Meier, J. Angonga, B. Gadway, Correlated dynamics in a synthetic lattice of momentum states, *Phys. Rev. Lett.* **120**, 040407 (2018).
- [55] J. Li *et al*, Spin-Orbit Coupling and Spin Textures in Optical Superlattices, *Phys. Rev. Lett.* **117**, 185301 (2016).
- [56] K. Sun, C. Qu, and C. Zhang, Spin-orbital-angular-momentum coupling in Bose-Einstein condensates, *Phys. Rev. A* **91**, 063627 (2015).
- [57] M. DeMarco, and H. Pu, Angular spin-orbit coupling in cold atoms, *Phys. Rev. A* **91**, 033630 (2015).
- [58] C. Qu, K. Sun, and C. Zhang, Quantum phases of Bose-Einstein condensates with synthetic spin-orbital-angular-momentum coupling, *Phys. Rev. A* **91**, 053630 (2015).

Supplementary materials

Single particle Hamiltonian

Here we derive the single-particle Hamiltonian of Eq. (2) in the main text using adiabatic elimination and the rotating wave approximation. The atomic lambda system consists of two atomic hyperfine ground states, denoted as $|\uparrow\rangle$, $|\downarrow\rangle$, and an excited state $|e\rangle$. The system is driven by two pairs of off-resonance lasers (ω_a, ω_b) and $(\omega_{a'}, \omega_{b'})$, as illustrated in Fig. 1(b, c) (main text). The frequency $\omega_{a'}$ ($\omega_{b'}$) is shifted by $\Delta' \sim 100$ MHz from ω_a (ω_b) so that the interference effects can be neglected and the two pairs can be treated individually. The frequency of each Raman laser satisfies $\delta_a = \omega_{e\uparrow} - \omega_a$ and $\delta_b = \omega_{e\downarrow} - \omega_b$, where $\omega_{e\uparrow}$ ($\omega_{e\downarrow}$) is the energy difference between $|e\rangle$ and $|\uparrow\rangle$ ($|\downarrow\rangle$). In the rotating frame defined by the transition $\begin{pmatrix} |\uparrow\rangle \\ |\downarrow\rangle \\ |e\rangle \end{pmatrix} \rightarrow e^{i\widehat{R}_1} \begin{pmatrix} |\uparrow\rangle \\ |\downarrow\rangle \\ |e\rangle \end{pmatrix}$, where $\widehat{R}_1 = \text{diag}(\delta/2, \omega_\uparrow - \omega_\downarrow - \delta/2, \omega_\uparrow - \omega_e + \Delta)$ with $\delta = \delta_a - \delta_b$ and $\Delta = (\delta_a + \delta_b)/2$, the laser-atom interaction Hamiltonian becomes [49]

$$H_{\text{LA}} = \begin{pmatrix} -\frac{\delta}{2} & 0 & \frac{\Omega_a^*}{2} \left(1 + \frac{\Omega_{a'}^*}{\Omega_a^*} e^{i(\omega_{a'} - \omega_a)t}\right) \\ 0 & \frac{\delta}{2} & \frac{\Omega_b^*}{2} \left(1 + \frac{\Omega_{b'}^*}{\Omega_b^*} e^{i(\omega_{b'} - \omega_b)t}\right) \\ \frac{\Omega_a}{2} \left(1 + \frac{\Omega_{a'}}{\Omega_a} e^{i(\omega_a - \omega_{a'})t}\right) & \frac{\Omega_b}{2} \left(1 + \frac{\Omega_{b'}}{\Omega_b} e^{i(\omega_b - \omega_{b'})t}\right) & \Delta \end{pmatrix}.$$

Here Ω_i is the Rabi coupling strength. Since $\Delta \gg |\delta|, |\Omega_i|$, the excited state can be adiabatic eliminated, yielding

$$H_{\text{LA}}^{\text{eff}} = \begin{pmatrix} -\delta/2 & \frac{\tilde{\Omega}_a \tilde{\Omega}_b^*}{2\Delta} \\ \frac{\tilde{\Omega}_a^* \tilde{\Omega}_b}{2\Delta} & \delta/2 \end{pmatrix},$$

where $\tilde{\Omega}_a = \Omega_a \left(1 + \frac{\Omega_{a'}}{\Omega_a} e^{i\tilde{\omega}_a t}\right)$ and $\tilde{\Omega}_b = \Omega_b \left(1 + \frac{\Omega_{b'}}{\Omega_b} e^{i\tilde{\omega}_b t}\right)$ with $\tilde{\omega}_i = \omega_{i'} - \omega_i$. Taking $\tilde{\omega}_a = \tilde{\omega}_b$ (i.e., the two pairs of Raman lasers have the same frequency difference) and neglecting fast time modulating terms, the Raman coupling becomes $\tilde{\Omega}_a \tilde{\Omega}_b^* = \Omega_a \Omega_b^* + \Omega_{a'} \Omega_{b'}^*$, which is a direct summation of Raman couplings for each laser pair. Considering the laser configuration in Fig. 1 of the main text, we have

$$H_V = \frac{(\hbar k_x)^2}{2m} + \frac{1}{2} \begin{pmatrix} -\delta & \Omega e^{-2ik_R x} + 2e^{i\phi_L} \Omega_L e^{-2i(k_R - k_L)x} \\ \Omega e^{2ik_R x} + 2e^{-i\phi_L} \Omega_L e^{2i(k_R - k_L)x} & \delta \end{pmatrix},$$

where ϕ_L is the phase difference between the two Raman couplings and $k_L < k_R$ since the primed lasers are injected at an angle θ_L . A standard unitary transformation of the spatially dependent phases yields the single particle Hamiltonian

$$H_0 = \frac{1}{2} \begin{pmatrix} \frac{\hbar^2}{m} (k_x - k_R)^2 - \delta & \Omega + e^{i\phi_L} 2\Omega_L e^{2ik_L x} \\ \Omega + e^{-i\phi_L} 2\Omega_L e^{-2ik_L x} & \frac{\hbar^2}{m} (k_x + k_R)^2 + \delta \end{pmatrix}.$$

2-level approximation and Rabi oscillation

The second pair of Raman lasers can induce coupling between the k and $k \pm 2k_L$ states with different spins in the SOC picture. Taking only the 6 most relevant neighboring states around the two band minima, the single particle Hamiltonian can be projected to

$$H = \begin{pmatrix} (-1 + 3k_L)^2 & 0 & 0 & \Omega_L e^{i\phi_L} & 0 & 0 \\ 0 & (-1 + k_L)^2 & 0 & \Omega/2 & \Omega_L e^{i\phi_L} & 0 \\ 0 & 0 & (-1 - k_L)^2 & 0 & \Omega/2 & \Omega_L e^{i\phi_L} \\ \Omega_L e^{-i\phi_L} & \Omega/2 & 0 & (1 + k_L)^2 & 0 & 0 \\ 0 & \Omega_L e^{-i\phi_L} & \Omega/2 & 0 & (1 - k_L)^2 & 0 \\ 0 & 0 & \Omega_L e^{-i\phi_L} & 0 & 0 & (1 - 3k_L)^2 \end{pmatrix},$$

where we have set $k_R = 1$ and rearranged the order to put states with the same spin together. Using the relation $k_L = \sqrt{1 - (\frac{\Omega}{4})^2}$, we can diagonalize the Hamiltonian with $\Omega_L = 0$, yielding the bare Hamiltonian

$H_B = \text{diag}((1 - 3k_L)^2, -1 + k_L^2, 3 + k_L^2, 3 + k_L^2, -1 + k_L^2, (1 - 3k_L)^2)$ for the SOC band. The corresponding states are labeled from $|1\rangle$ to $|6\rangle$ in Fig. 2(c). In this new basis, the total Hamiltonian can be rewritten as $H_B + \Omega_L H'$ with

$$H' = \begin{pmatrix} 0 & \sqrt{\frac{1-k_L}{2}} e^{i\phi_L} & 0 & \sqrt{\frac{1+k_L}{2}} e^{i\phi_L} & 0 & 0 \\ \sqrt{\frac{1-k_L}{2}} e^{-i\phi_L} & 0 & -\frac{1}{2}\sqrt{1-k_L^2} e^{i\phi_L} & 0 & -\frac{1}{2}(1+k_L) e^{i\phi_L} & 0 \\ 0 & -\frac{1}{2}\sqrt{1-k_L^2} e^{-i\phi_L} & 0 & -\frac{1}{2}(-1+k_L) e^{-i\phi_L} & 0 & \sqrt{\frac{1+k_L}{2}} e^{i\phi_L} \\ \sqrt{\frac{1+k_L}{2}} e^{-i\phi_L} & 0 & -\frac{1}{2}(-1+k_L) e^{i\phi_L} & 0 & \frac{1}{2}\sqrt{1-k_L^2} e^{i\phi_L} & 0 \\ 0 & -\frac{1}{2}(1+k_L) e^{-i\phi_L} & 0 & \frac{1}{2}\sqrt{1-k_L^2} e^{-i\phi_L} & 0 & -\sqrt{\frac{1-k_L}{2}} e^{i\phi_L} \\ 0 & 0 & \sqrt{\frac{1+k_L}{2}} e^{-i\phi_L} & 0 & -\sqrt{\frac{1-k_L}{2}} e^{-i\phi_L} & 0 \end{pmatrix}.$$

Clearly, the coupling between the two band minima 2 and 5 with energy $-1 + k_L^2$ is $V = -\frac{\Omega_L}{2}(1 + k_L)e^{\mp i\phi_L}$. Note that, we only compute the coupling strength to the first-order of Ω_L , and one may come to the same conclusion even using a minimal four-level model (two minima and corresponding upper band states).

We neglect other state populations and thus project the Hamiltonian onto a two-level model in Eq.(3). Without interaction, the single particle Hamiltonian in this 2-level approximation is rewritten as (without loss of generality, we set $\phi_L = 0$)

$$H = -k_L \delta \tau_z - V_0 \tau_x = \omega (-\cos \alpha \tau_z + \sin \alpha \tau_x),$$

where $\tan \alpha = -V_0/(k_L \delta)$ and $\{\tau\}$ are Pauli matrices. The oscillation of any state driven by this Hamiltonian can be calculated using the time-evolution operator,

$$e^{-iHt} = \begin{pmatrix} \cos \omega t + i \cos \alpha \sin \omega t & -i \sin \alpha \sin \omega t \\ -i \sin \alpha \sin \omega t & \cos \omega t - i \cos \alpha \sin \omega t \end{pmatrix}.$$

For a general state at $t = 0$ (an initial state can be analytically obtained using variational analysis and is discussed in the following section),

$$\psi(0) = \begin{pmatrix} \psi_2(0) \\ \psi_5(0) \end{pmatrix} = \begin{pmatrix} \cos(\theta/2) \\ -e^{i\gamma} \sin(\theta/2) \end{pmatrix},$$

we have

$$\begin{pmatrix} \psi_2(t) \\ \psi_5(t) \end{pmatrix} = e^{-iHt} \begin{pmatrix} \psi_2(0) \\ \psi_5(0) \end{pmatrix} = \begin{pmatrix} \cos \frac{\theta}{2} \cos \omega t + i \sin \omega t (\cos \frac{\theta}{2} \cos \alpha + e^{i\gamma} \sin \frac{\theta}{2} \sin \alpha) \\ -e^{i\gamma} \sin \frac{\theta}{2} \cos \omega t - i \sin \omega t (\cos \frac{\theta}{2} \sin \alpha - e^{i\gamma} \sin \frac{\theta}{2} \cos \alpha) \end{pmatrix},$$

from which we can compute the population or phase difference between two states at any time. The spin polarization is given by

$$\langle \sigma_z \rangle = \cos \theta + \sin \theta (\sin 2\alpha \sin^2 \omega t \cos \gamma - \sin \alpha \sin 2\omega t \sin \gamma),$$

which can be written in a sinusoidal form

$$\langle \sigma_z \rangle = \cos \theta + \frac{1}{2} \sin \theta \sin 2\alpha \cos \gamma - \sin \theta \sin \alpha \sqrt{\sin^2 \gamma + \cos^2 \alpha \cos^2 \gamma} \sin(2\omega t + \varphi_0),$$

with $\tan \varphi_0 = \cos \alpha \cot \gamma$. The Rabi oscillation period is clearly $T = \pi/\omega$, which is independent of initial states for non-interacting cases within the 2-level approximation.

It is well known that such Rabi oscillation in a two-level system can be understood as the precession of a magnetic moment in a magnetic field. For $\phi_L = 0$, the effective magnetic field lies in the x - z plane with strength ω and angle $\alpha = \arctan \frac{V_0}{k_L \delta}$ from the z -axis. A non-zero ϕ_L simply gives it a y component. Both tunneling-phase-driven and voltage-driven processes are illustrated in Fig. 6. Since ϕ is defined in the x - y plane, the system will undergo a Josephson oscillation when the origin is enclosed by the projection of the precessing trajectories on the x - y plane. A non-zero detuning is preferred for the oscillation even for the tunneling-phase-driven process because ϕ may otherwise only jump between $\pm\pi$.

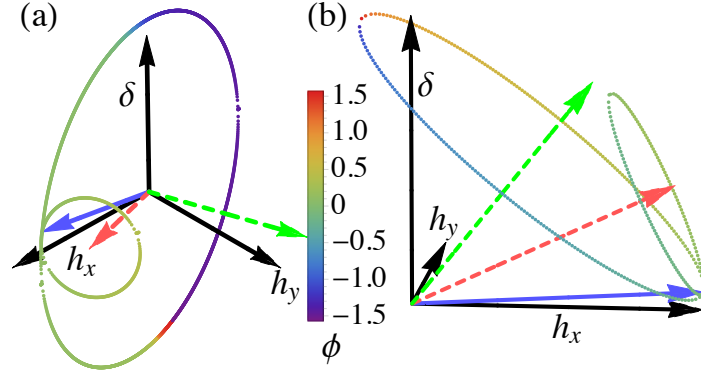


FIG. 6: (Color online) Cartoon illustration of the quench dynamics when interaction is weak compared to the coupling strength. Blue solid arrow denotes the orientation of the initial state, while the two dashed arrows (red and green) denote the orientation of the effective magnetic fields after a quench for plasma and Josephson oscillations, respectively. The circles give the trajectories of moment precession and the color shows the relative phase ϕ , which is defined in the h_x - h_y plane. (a) Tunneling-phase-driven MSJJ. The arrows can have arbitrary orientation in space. (b) Voltage-driven MSJJ. The arrows are confined in a plane, where their angles to h_x remain a constant (for this panel, the angle is simply 0).

Variational analyses

The atomic interaction can be described in the mean field approximation by

$$H_I = \frac{1}{2} \int dx [g_{\uparrow\uparrow} |\psi_{\uparrow}|^4 + g_{\downarrow\downarrow} |\psi_{\downarrow}|^4 + 2g_{\uparrow\downarrow} |\psi_{\uparrow}|^2 |\psi_{\downarrow}|^2].$$

In the following discussions, we assume $g_{\uparrow\uparrow} \sim g_{\downarrow\downarrow} \sim g$. The spinor wave function considered here is

$$\begin{pmatrix} \psi_{\uparrow} \\ \psi_{\downarrow} \end{pmatrix} = \sqrt{n} \left(C_2 \begin{pmatrix} \cos \theta \\ -\sin \theta \end{pmatrix} e^{ik_1 x} + C_5 \begin{pmatrix} \sin \theta \\ -\cos \theta \end{pmatrix} e^{-ik_1 x} \right)$$

where $2\theta = \arccos(k_1/k_R)$ can be solved from minimizing the single particle energy. The energy density given by this spinor wavefunction is [46]

$$\epsilon = \frac{1}{2} k_R^2 - \frac{1}{2} \Omega \sin 2\theta - \Omega_L \cos^2 \theta (C_2^* C_5 e^{i\phi_L} + C_2 C_5^* e^{-i\phi_L}) \delta_{k_1, k_L} - \frac{\delta}{2} (|C_2|^2 - |C_5|^2) - F \frac{k_1^2}{2k_R^2} + G_1 (1 + 2|C_2|^2 |C_5|^2),$$

where $F = (k_R - 2G_2)^2 + 4(G_1 + 2G_2)|C_2|^2 |C_5|^2$, $G_1 = n(g + g_{\uparrow\downarrow})/4$, and $G_2 = n(g - g_{\uparrow\downarrow})/4$.

Through variational methods, one can find $k_1 = k_R \sqrt{1 - \Omega^2/(4F)^2}$. The equation of motion in the main text can be obtained by computing the variation of the energy functional with respect to C_2 and C_5 , with

$$g_G = -4G_2 + \frac{1}{2} \Omega^2 \frac{(G_1 + 2G_2)(k_R - 2G_2)}{\left(\frac{k_R - 2G_2}{|C_2|^2 |C_5|^2} + 4|C_2|^2 |C_5|^2 (G_1 + 2G_2) \right)^3},$$

which is dependent on the product $|C_2|^2 |C_5|^2$. However, the dependency can be eliminated when the interaction strength is weak compared to E_R , i.e., $G_i \ll k_R$, yielding $g_G = 2G_1 - 2(k_1^2/k_R^2)(G_1 + 2G_2)$. Taking $C_j = \sqrt{N_j} e^{i\theta_j}$, $j = \{2, 5\}$ and in terms of the phase difference $\phi = \theta_2 - \theta_5$ and fractional population difference $z = \frac{N_2 - N_5}{N}$, we obtain the classical equations of motions in the main text

$$\begin{aligned} \partial_t z &= -\sqrt{1 - z^2} \sin(\phi - \phi_{Lf}), \\ \partial_t \phi &= \frac{g_G}{V_0} z + \frac{z}{\sqrt{1 - z^2}} \cos(\phi - \phi_{Lf}) + \frac{k_L \delta}{V_0}, \end{aligned}$$

where time has been rescaled as $t \rightarrow 2V_0 t$. As long as the detuning after the quench is large enough, the system is ensured to experience a Josephson oscillation as $\phi \sim (k_L \delta / V_0) t$. The classical Hamiltonian can be found through the conjugate relation $\partial_t z = -\frac{\partial H_c}{\partial \phi}$ and $\partial_t \phi = \frac{\partial H_c}{\partial z}$,

$$H_c = \frac{g_G}{2V} z^2 - \sqrt{1 - z^2} \cos(\phi - \phi_{Lf}) + \frac{k_L \delta}{V_0} z + H_{c0},$$

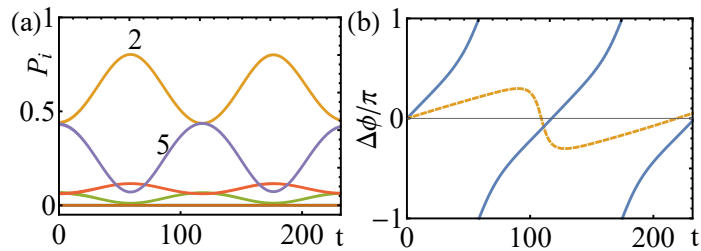


FIG. 7: (Color online) Similar as Fig. 3 (a) and (b), but for a voltage-driven MSJJ.

where H_{c0} is an integration constant.

Voltage-driven MSJJ

The GPE simulation results for a voltage(detuning)-driven Josephson oscillation are shown in Fig. 7(a), indicating that our 2-state approximation still works. The parameters are chosen as $\Omega = 2.7$, $\Omega_L = 0.015$, $\phi = 0$ and $ng = 0.07$, while δ is quenched from 0 Hz to 0.054. The evolution of its phase difference is plotted in Fig. 7(b) as the blue curves. For comparison, we also present the phase difference for plasma oscillation, where all the parameters are the same, except that δ is quenched to 0.016. Similar self-trapping effects may also be observed when δ is quenched from a finite value to 0. A constant π -oscillation occurs when $\phi_L = \pi/2$ and δ is quenched from a small number to 0 (to ensure symmetric oscillation). In this case, the phase difference is almost a constant at $\pi/2$, while the polarization oscillates symmetrically with an observable amplitude.

Numerical methods

In the numerical simulation, we consider a 1D BEC in a harmonic trap with spin-orbit coupling and Raman-assisted tunneling. The system is described by the GPE (1) in the main text. We use imaginary-time evolution to obtain the ground state numerically with a time-split-operator numerical method [50] (see [48] for alternative methods). The resulting phase diagram is compared with that generated through variational analysis. The dynamics are studied through real-time evolution of the ground state and the time interval δt for each evolution step is reduced until the final state after time T has converged. In our simulation, the real-space wavefunction is sampled by 2^{11} points, and the ground state energy is achieved to a precision up to 10^{-9} . We choose $\delta t = 0.01$ for each step in the real-time evolution.